Research Article

High-entropy $(La_{0.2}Nd_{0.2}Sm_{0.2}Eu_{0.2}Gd_{0.2})_2Ce_2O_7$: A potential thermal barrier material with improved thermo-physical properties

Yun XUE[a,b], Xiaoqin ZHAO[a,b], Yulong AN[a,b,*], Yijing WANG[a,b],
Meizhen GAO[c], Huidi ZHOU[a,b], Jianmin CHEN[a,b]

[a]*Key Laboratory of Science and Technology on Wear and Protection of Materials, Lanzhou Institute of Chemical Physics, Chinese Academy of Sciences, Lanzhou 730000, China*
[b]*Center of Materials Science and Optoelectronics Engineering, University of Chinese Academy of Sciences, Beijing 100049, China*
[c]*Key Lab for Magnetism and Magnetic Materials of MOE, School of Physical Science and Technology, Lanzhou University, Lanzhou 730000, China*

Abstract: High-entropy oxides (HEOs) are widely researched as potential materials for thermal barrier coatings (TBCs). However, the relatively low thermal expansion coefficient (TEC) of those materials severely restricts their practical application. In order to improve the poor thermal expansion property and further reduce the thermal conductivity, high-entropy $(La_{0.2}Nd_{0.2}Sm_{0.2}Eu_{0.2}Gd_{0.2})_2Ce_2O_7$ is designed and synthesized in this work. The as-prepared multicomponent material is formed in a simple disordered fluorite structure due to the high-entropy stabilization effect. Notably, it exhibits a much higher TEC of approximately 12.0×10^{-6} K^{-1} compared with those of other high-entropy oxides reported in the field of TBCs. Besides, it presents prominent thermal insulation behavior with a low intrinsic thermal conductivity of 0.92 $W \cdot m^{-1} \cdot K^{-1}$ at 1400 ℃, which can be explained by the existence of high concentration oxygen vacancies and highly disordered arrangement of multicomponent cations in the unique high-entropy configuration. Through high-temperature *in-situ* X-ray diffraction (XRD) measurement, this material shows excellent phase stability up to 1400 ℃. Benefiting from the solid solution strengthening effect, it shows a higher hardness of 8.72 GPa than the corresponding single component compounds. The superior thermo-physical performance above enables $(La_{0.2}Nd_{0.2}Sm_{0.2}Eu_{0.2}Gd_{0.2})_2Ce_2O_7$ a promising TBC material.

Keywords: high-entropy oxides (HEOs); $(La_{0.2}Nd_{0.2}Sm_{0.2}Eu_{0.2}Gd_{0.2})_2Ce_2O_7$; defective fluorite structure; thermal expansion coefficient (TEC); thermal conductivity; thermal barrier coating (TBC)

1 Introduction

Inspired by the remarkable research developments in

* Corresponding author.
E-mail: anyulong@licp.cas.cn

high-entropy alloys (HEAs), Rost *et al.* [1] first extended high-entropy materials to high-entropy oxides (HEOs) in 2015, which belong to the family of high-entropy ceramics (HECs). Since then, much attention has been attracted to deep exploration of HECs including high-entropy carbides [2–4], high-

entropy nitrides [5], high-entropy borides [6,7], high-entropy sulfides [8], and high-entropy silicides [9,10]. Currently, there is no specific definition for HECs, while Xiang *et al.* [11] defined them as multi-principal-component solid solutions in which the near-equiatomic cations share one or more Wyckoff sites simultaneously. Among the various high-entropy materials, HEOs have aroused extensive research interest. Owing to the distinctive structures and tunable properties, HEOs exhibit great prospective applications, such as in the field of supercapacitors [5], Li-ion batteries [12–14], and thermoelectrics [15], especially in thermal barrier coatings (TBCs) [16–19].

TBCs are essential parts of the hot end components in gas turbine. The gas inlet temperature of these hot end parts has already exceeded the maximum service temperature (no more than 1150 ℃) of nickel-based superalloys, which are used to prepare turbine blades and other hot end components [19]. Thus, researchers extensively exploit TBCs to protect the superalloys from ultra-high working temperature. Benefiting from the relatively low thermal conductivity (2.40 W·m^{-1}·K^{-1} at 1000 ℃) [20], 6–8 wt% yttria-stabilized zirconia (YSZ) has been widely applied as a kind of commercial TBCs. Besides, YSZ possesses a high thermal expansion coefficient (TEC) of 10.9×10^{-6} K^{-1} [21], superior fracture toughness (~3 MPa·m$^{1/2}$) [22], and low Young's modulus (~240 GPa) [23]. Unfortunately, the practical application of YSZ is seriously restricted by the phase transformation during the prolonged high-temperature service above 1200 ℃. The phase transformation always generates a heavy volume change to the material, and results in the spallation and failure of TBCs [24–26]. Hence, exploring new-type TBCs with higher temperature phase stability and lower thermal conductivity is urgently needed. Three mainstream strategies have been proposed to overcome such drawbacks over past decades: (i) introduction of doping additives into YSZ like gadolinia (Gd$_2$O$_3$) [27], neodymia (Nd$_2$O$_3$) [28], erbia (Er$_2$O$_3$) [29], and ytterbia (Yb$_2$O$_3$) [28] to mitigate the phase transformation; (ii) exploitation of other advanced materials for TBCs such as La$_2$Ce$_2$O$_7$ [30], Gd$_2$Zr$_2$O$_7$ [31], and DyTaO$_4$ [32]; (iii) construction of multi-layered TBC top coats via emerging thermal spray techniques including atmospheric plasma spraying (APS), suspension plasma spraying, and solution plasma spraying [19]. Based on the material design principles above, a considerable number of materials have been prepared by researchers, such as La$_2$Zr$_2$O$_7$ [33], LuTaO$_4$ [32], and rare earth silicates [16]. Currently, although there are enormous TBCs studied to improve the performance of conventional YSZ, it is still hard to fulfill the increasing demand of modern high efficiency gas turbine and jet.

In order to search for prospective TBCs with more superior performance, high-entropy ceramics have been designed and prepared in the past ten years. HECs are successfully confirmed to be a promising candidate for TBCs with lower thermal conductivity than their corresponding constituent materials. Such excellent thermal insulation property largely originates from the cocktail effect in high-entropy compound. The synergistic effect of multicomponent elements would arouse unexpected improvements in thermo-physical properties. In addition, due to the high entropy effect and sluggish diffusion effect, HECs possess outstanding phase stability and low grain growth rate. Excellent thermal insulation property is vitally important to TBCs. In nonmagnetic insulating ceramics, the contribution of electron and magnon to heat conduction can be neglected. Thus, the thermal conductivity of HECs is mainly determined by phonon scattering, including intrinsic scattering between phonons, lattice defect scattering, grain boundary scattering in polycrystalline materials, etc. The ideal structure of HECs usually contains a cation sub-lattice with long-range periodicity but compositional disorder [34]. The novel incorporation ways of multi-component cations in HECs produce significant differences in atomic mass, ionic radius, and interatomic force, which create severe lattice distortion and largely enhance phonon scattering. As a result, the thermal conductivity is reduced to a great extent. For instance, five different HEOs are designed with six cations, Mg$_x$Ni$_x$Cu$_x$Co$_x$Zn$_x$M$_x$O, x = 0.167, where M represents for Sc, Sb, Sn, Cr, and Ge. Through experiment and simulation results, they demonstrate that the lower thermal conductivity of the as-prepared HEOs without sacrificing mechanical stiffness is probably from the highly disordered interatomic force among the ionic bonds [35]. Moreover, high-entropy (La$_{0.2}$Ce$_{0.2}$Nd$_{0.2}$Sm$_{0.2}$Eu$_{0.2}$)$_2$Zr$_2$O$_7$ is also considered as a potential thermal insulation material due to the low thermal conductivity of 2.06±0.06 W·m^{-1}·K^{-1} at room temperature [36] and slow grain growth rate [37]. In addition to zirconates, a recent work reported a high-entropy (Y$_{0.2}$Yb$_{0.2}$Lu$_{0.2}$Eu$_{0.2}$Er$_{0.2}$)$_3$Al$_5$O$_{12}$ ceramic with good thermal stability and outstanding chemical

compatibility with thermally grown Al_2O_3 [38]. It exhibits a close TEC ($(8.54\pm0.29) \times 10^{-6}$ K^{-1} at 673–1273 K) to that of Al_2O_3 and a low thermal conductivity. $(Sm_{0.2}Eu_{0.2}Tb_{0.2}Dy_{0.2}Lu_{0.2})_2Ce_2O_7$ and $(Sm_{0.2}Eu_{0.2}Tb_{0.2}Dy_{0.2}Lu_{0.2})_2ZrCeO_7$ are also studied with a low conductivity around 1.2 $W\cdot m^{-1}\cdot K^{-1}$ at 1000 ℃ [39].

Up to now, a series of high-entropy materials have been investigated in the field of TBCs. However, the relatively high thermal conductivity and low TEC of those materials severely restrict their practical applications. The research on thermal contraction behavior of cerium oxide-based high-entropy oxides is still a lack of deep study. To address these problems, a new high-entropy ceramic $(La_{0.2}Nd_{0.2}Sm_{0.2}Eu_{0.2}Gd_{0.2})_2Ce_2O_7$ with fluorite structure is designed and successfully synthesized in this work. The as-prepared material shows a low intrinsic thermal conductivity of 0.92 $W\cdot m^{-1}\cdot K^{-1}$ at 1400 ℃. Besides, this material exhibits a relatively high TEC of approximately 12.0×10^{-6} K^{-1}. Meanwhile, through high-temperature *in-situ* X-ray diffraction (XRD) measurement, the material shows excellent phase stability up to 1400 ℃. As TBC material, $(La_{0.2}Nd_{0.2}Sm_{0.2}Eu_{0.2}Gd_{0.2})_2Ce_2O_7$ manifests obvious improvement compared with that of other single component rare-earth cerates reported in the literature. Such prominent thermo-physical properties largely attribute to the cocktail effect of high-entropy material, which combine the properties of the constituent components and eventually exceed them. This work further enriches the research content for the family of high-entropy materials.

2 Experimental

2.1 Preparation of high-entropy $(La_{0.2}Nd_{0.2}Sm_{0.2}Eu_{0.2}Gd_{0.2})_2Ce_2O_7$ powders and bulks

The dense $(La_{0.2}Nd_{0.2}Sm_{0.2}Eu_{0.2}Gd_{0.2})_2Ce_2O_7$ bulk was prepared by a two-step solid reaction method. All chemicals employed in this work were of analytical grade from Macklin Biochemical Technology Co., Ltd., Shanghai, China and used directly without further treatment. The experimental process was illustrated in Fig. 1. Firstly, rare earth powders of La_2O_3, Nd_2O_3, Sm_2O_3, Eu_2O_3, Gd_2O_3, and CeO_2 were weighed in stoichiometric ratio and mixed with anhydrous ethyl alcohol through ball milling for 24 h at 400 $r\cdot min^{-1}$. The obtained slurry was dried in oven at 70 ℃ for 10 h and collected after sieving by 40-mesh sieve. Then the resulting powders were pre-sintered at different temperatures (1250, 1300, 1350, 1400, and 1480 ℃) for 2 h to get pure single-phase sample. After cooling, the samples were broken into powders and ball milled for another 24 h at 400 $r\cdot min^{-1}$ followed by drying in oven at 70 ℃ for 10 h.

The completely dried powders were screened through 40 meshes and pressed into columnar shaped compacts of 12 mm in diameter and 3 mm in height under a force of 9 t. Finally, the green bodies were sintered at 1480 ℃ for 3 h to get dense bulk $(La_{0.2}Nd_{0.2}Sm_{0.2}Eu_{0.2}Gd_{0.2})_2Ce_2O_7$ ceramics.

2.2 Characterizations

The crystal structures of the as-prepared samples were

Fig. 1 Preparation process of high-entropy $(La_{0.2}Nd_{0.2}Sm_{0.2}Eu_{0.2}Gd_{0.2})_2Ce_2O_7$.

characterized by XRD (Smartlab-SE, Rigaku, Japan) with a step width of 0.01° ranging from 20° to 80°. High-temperature *in-situ* XRD system (D8 Advance, Bruker, Germany) was employed to analyze the phase transformation and lattice evolution during the temperature-increasing process. Microstructure morphology and element distribution of $(La_{0.2}Nd_{0.2}Sm_{0.2}Eu_{0.2}Gd_{0.2})_2Ce_2O_7$ pre-sintered powders as well as that of dense bulk were investigated with field emission environmental scanning electron microscope (SEM; Quanta 650 FEG, FEI, USA). In addition, the high resolution microstructure of bulk $(La_{0.2}Nd_{0.2}Sm_{0.2}Eu_{0.2}Gd_{0.2})_2Ce_2O_7$ was studied by a transmission electron microscope (TEM; TECNAI G2 F20 S-TWIN, FEI, USA). Here, the sample used in TEM test was prepared via the focused ion beam (FIB; Helios G4, Waltham, USA). The lattice parameters and theoretical density were calculated according to the XRD Rietveld refinement and TEM analysis. The data for the refinement was tested in a step width of 0.02° and 4 s·step^{-1}.

Microhardness tester (MH-5-VM microhardness tester, Shanghai Heng Yi Technology Company, China) was used to measure the hardness of the $(La_{0.2}Nd_{0.2}Sm_{0.2}Eu_{0.2}Gd_{0.2})_2Ce_2O_7$ at a load of 1000 g. Before testing, the sample was carefully polished by diamond abrasives. In order to minimize the experimental error, the sample was measured five times to calculate the average value.

The density (ρ) of the bulk specimen was tested by Archimedes' method. In the measurement of thermal diffusivities (λ), the sample was cut into a size of ϕ 10 mm × 3 mm disc and evaporated with gold and graphite on both sides to protect the sample from laser reflection of ion beam and weaken the high-temperature heat radiation. This test was carried out by high-temperature laser thermal conduction analyzer (DLF2800, TA, USA) from room temperature to 1400 ℃. Then the thermal conductivity (κ') can be calculated by Eq.(1):

$$\kappa' = \lambda \times C_p \times \rho \tag{1}$$

where C_p represents the heat capacity computed by Neumann–Kopp rule.

In order to eliminate the effect of porosity, the thermal conductivity was corrected by Eq. (2) [40]:

$$\kappa'/\kappa = 1 - 4\varphi/3 \tag{2}$$

where κ is the thermal conductivity of the fully dense sample, φ is the porosity of the as-synthesized materials, which is determined by the ratio of experimental density and theoretical density.

Besides, the TEC was obtained by thermal dilatometer

(DIL402 E, Netzsch, Germany) under the protection of argon flow. The bulk $(La_{0.2}Nd_{0.2}Sm_{0.2}Eu_{0.2}Gd_{0.2})_2Ce_2O_7$ was prepared in a rectangular shape of 5 mm × 5 mm × 25 mm.

3 Results and discussion

3. 1 Characterization of high-entropy $(La_{0.2}Nd_{0.2}Sm_{0.2}Eu_{0.2}Gd_{0.2})_2Ce_2O_7$ powders

Figure 2(a) displays the XRD patterns of the pre-sintered $(La_{0.2}Nd_{0.2}Sm_{0.2}Eu_{0.2}Gd_{0.2})_2Ce_2O_7$ powders under different temperatures accompanied by the standard PDF card of $La_2Ce_2O_7$ (PDF#04-012-6396). It can be seen that the diffraction peaks of the powders are similar to those of $La_2Ce_2O_7$ with a disordered defective fluorite structure, which belongs to the space group of $Fm\bar{3}m$ (225). Here, the high entropy effect contributes to the formation of simple-phase solid solution. Besides, it was reported that the components of compounds with $A_2B_2O_7$ formula (A = La^{3+}, Nd^{3+}, Sm^{3+}, Eu^{3+}, Gd^{3+}, etc.; B = Ce^{4+}, Zr^{4+}, etc.) generally possess ordered pyrochlore structure (cubic, $Fd\bar{3}m$) and disordered defective fluorite structure (cubic, $Fm\bar{3}m$) [41]. When the radius ratio of R_A/R_B locates in the range of 1.46–1.78, the sample will stabilize in pyrochlore structure. While R_A/R_B lies below the low limit of 1.46, the compound is prone to forming in a fluorite structure [42]. The ionic radii of cations used in this work are summarized in Table 1, where the radius of Ln^{3+} (Ln = La^{3+}, Nd^{3+}, Sm^{3+}, Eu^{3+}, and Gd^{3+}) represents the
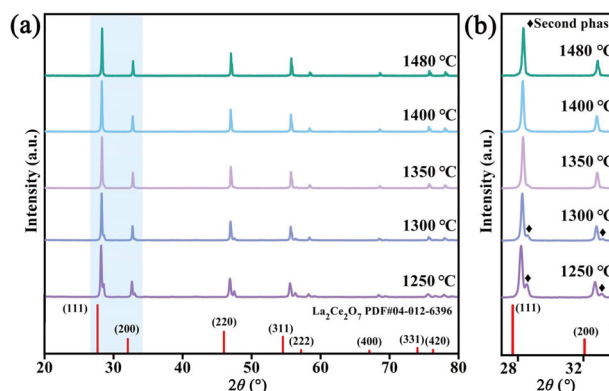
Fig. 2 XRD patterns of pre-sintered $(La_{0.2}Nd_{0.2}Sm_{0.2}Eu_{0.2}Gd_{0.2})_2Ce_2O_7$ powders: (a) $20° \leqslant 2\theta \leqslant 80°$; (b) characteristic peaks of $27° \leqslant 2\theta \leqslant 34°$.

Table 1   Ion radii of different ions in Ref. [43]

Ion	Ce^{4+}	La^{3+}	Nd^{3+}	Sm^{3+}	Eu^{3+}	Gd^{3+}	Ln^{3+}
Radius (nm)	0.0870	0.1160	0.1109	0.1079	0.1066	0.1053	0.1093

average ion radius of these five ions [43]. The effective ratio of R_A/R_B is calculated to be 1.26, which is greatly lower than 1.46 [44]. Thus, the designed compound $(La_{0.2}Nd_{0.2}Sm_{0.2}Eu_{0.2}Gd_{0.2})_2Ce_2O_7$ will be theoretically inclined to form fluorite structure, which is entirely consistent with the experimental results above. Besides, as can be seen obviously from the enlarged XRD pattern in Fig. 2(b), the main phase basically formed at 1250 ℃ with little amount of impurity, which possibly attributes to the residual solid solution CeO_2. With the increase of the temperature, the peak intensity of impurities declines gradually from 1300 ℃, and completely disappears at 1350 ℃. As the temperature rises from 1350 to 1480 ℃, the XRD patterns of the as-synthesized material show a single-phase structure with no impurities detected. An optimal pre-sintering temperature is extremely crucial for the preparation of dense ceramic bulk. Therefore, 1300 ℃ is determined as an appropriate temperature for pre-sintering powders in the first step. It guarantees the main phase formation of $(La_{0.2}Nd_{0.2}Sm_{0.2}Eu_{0.2}Gd_{0.2})_2Ce_2O_7$, which can prevent bulk crack and contraction in the calcination process due to the diminishing of thermal stress. Additionally, the high sintering activity of the powders obtained under 1300 ℃ facilitates the formation of dense bulk ceramics at a higher sintering temperature.

In order to study the morphology and element distribution of the as-synthesized $(La_{0.2}Nd_{0.2}Sm_{0.2}Eu_{0.2}Gd_{0.2})_2Ce_2O_7$ powders, the SEM–EDS measurement is performed. As displayed in the enlarged inset of Fig. 3(a), the particles present flake-like shapes with sizes ranging from 300 to 700 nm. In addition, as can be seen from Figs. 3(b)–3(h), all the elements are homogeneously distributed without any element enrichment. EDS test is also employed to detect the element content for the area in Fig. 3(a). According to the analysis results, the atomic fractions of each element are summarized in Fig. 3(i). The bar charts in orange illustrate the proportions of five Ln^{3+}, which are about 3.8% with a variation of ±0.2%. The extremely close atomic fraction of the five elements further demonstrates the equiatomic composition of Ln^{3+} at A site ($A_2B_2O_7$).
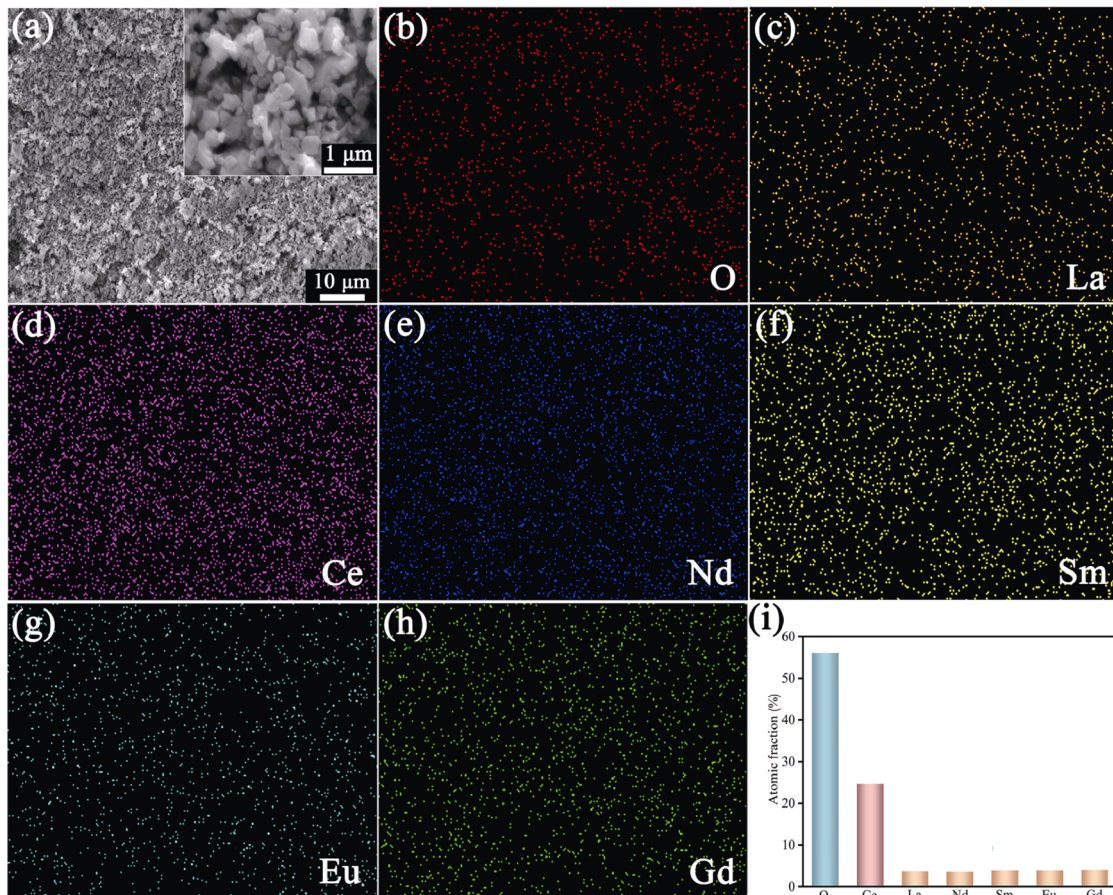
Fig. 3 (a) SEM image of $(La_{0.2}Nd_{0.2}Sm_{0.2}Eu_{0.2}Gd_{0.2})_2Ce_2O_7$ powders; (b–h) corresponding EDS mappings of O, La, Ce, Nd, Sm, Eu, and Gd elements, respectively; (i) atomic fraction of pre-sintered powders.

3. 2 Structure analysis of bulk high-entropy $(La_{0.2}Nd_{0.2}Sm_{0.2}Eu_{0.2}Gd_{0.2})_2Ce_2O_7$

The lattice structure of bulk $(La_{0.2}Nd_{0.2}Sm_{0.2}Eu_{0.2}Gd_{0.2})_2Ce_2O_7$ is characterized by XRD measurement with the testing results presented in Fig. 4. Standard XRD patterns of single component $Ln_2Ce_2O_7$ (Ln = La, Nd, Sm, Eu, and Gd) are displayed together for deep exploration of the structure formation. Similar to the results discussed above, the diffraction peaks of the bulk sample are well in line with the defective fluorite structure of $Ln_2Ce_2O_7$. The peak of (111) crystal plane is enlarged in Fig. 4(b). It is worth noting that all the corresponding peaks of our synthesized material deviate seriously towards the region of higher angle in comparison with that of single component $Ln_2Ce_2O_7$, which suggests a severe lattice distortion due to the size difference of five Ln^{3+}. Especially, the extent of peak shift becomes larger with the increase of 2θ. Such occurrence of peak shift is largely in account of cell shrinkage in the lattice structure. The lattice parameter (0.5477 nm) of the sample is obtained by the XRD refinement, and the result

is plotted in Fig. 4(c). As is shown that the calculated XRD pattern is fitted well with the experimental results. The weighted profile R value (R_{wp}) and statistically expected R value (R_{ep}) are lower than 15%, which indicates that the refined result is reliable.

The surface morphology and EDS mappings of bulk high-entropy $(La_{0.2}Nd_{0.2}Sm_{0.2}Eu_{0.2}Gd_{0.2})_2Ce_2O_7$ are presented in Fig. 5. As shown in Fig. 5(a), the average grain size is measured to be around 3.1 μm with clear grain boundary. Besides, there are no obvious pores observed in SEM images. The EDS mappings are displayed in Figs. 5(b)–5(h), where all the constituent elements space homogeneously without element enrichment. From the EDS analysis results of element content for the area in Fig. 5(a), the atomic fractions are plotted in Fig. 5(i). The 5 bar charts in grey color indicate an equal atomic fraction of the five Ln^{3+}, which is consistent well with the results of pre-sintered powders.

High resolution transmission electron microscopy (HRTEM) is employed to provide a deep insight into the detailed structure of $(La_{0.2}Nd_{0.2}Sm_{0.2}Eu_{0.2}Gd_{0.2})_2Ce_2O_7$. It can be seen in Fig. 6(a) that the planar spacing calculated to be 0.2741 nm matches well with (200) (d = 0.2739 nm) of fluorite structure in the testing result of XRD. Besides, from the selected area electron diffraction (SAED) patterns in the inset of Fig. 6(a), the angle between planes (220) and (200) calculated to be 46.31° is perfectly consistent with the results in HRTEM and XRD tests. All the discussions above confirm the perfect crystallinity of $(La_{0.2}Nd_{0.2}Sm_{0.2}Eu_{0.2}Gd_{0.2})_2Ce_2O_7$ with a defective fluorite structure.

Here, to obtain the relative density of our as-prepared bulk material, the cell volume can be calculated through interlayer distance from HRTEM, and thus the theoretical density is computed to be 6.96 g·cm^{-3}. As the practical density is tested to be 6.85 g·cm^{-3}, the bulk specimen exhibits a low porosity of about 1.6%. The theoretical density is consistent well with the result calculated in the XRD refinement (6.97 g·cm^{-3}).

The three-dimensional diagram of crystallographic structure is plotted to get an intensive insight into the high-entropy configuration in Fig. 6(b). It can be seen that five cations of Ln^{3+} and Ce^{4+} randomly distribute in the center of anion-coordinated cubic polyhedral, and the oxygen anions occupy the 8 corners of the cube at (1/4, 1/4, 1/4) of 8c site. Notably, 1/8 oxygen vacancy in white color appears at the same site with O^{2-} in order to get a charge balance for the whole
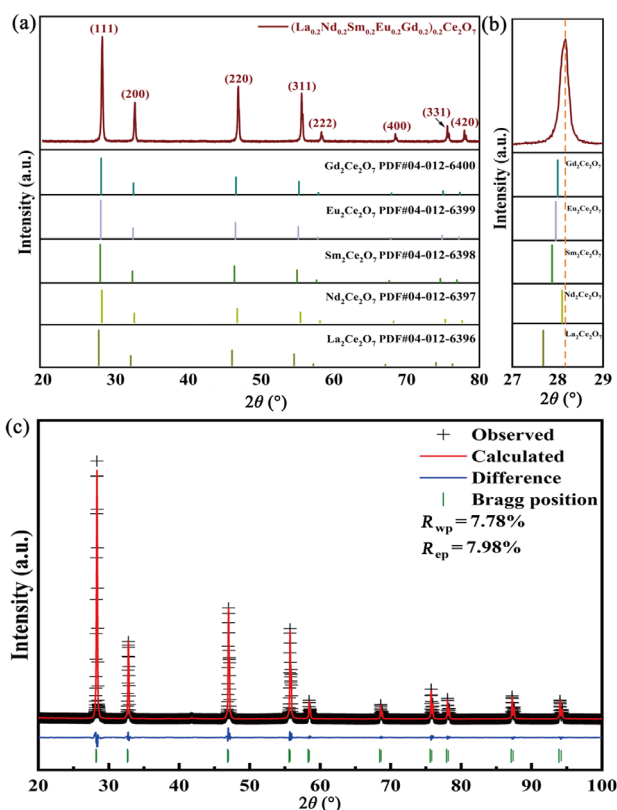
Fig. 4 (a) XRD patterns of bulk $(La_{0.2}Nd_{0.2}Sm_{0.2}Eu_{0.2}Gd_{0.2})_2Ce_2O_7$; (b) main peak shift of (111) crystal plane; (c) Rietveld refinement of XRD patterns.
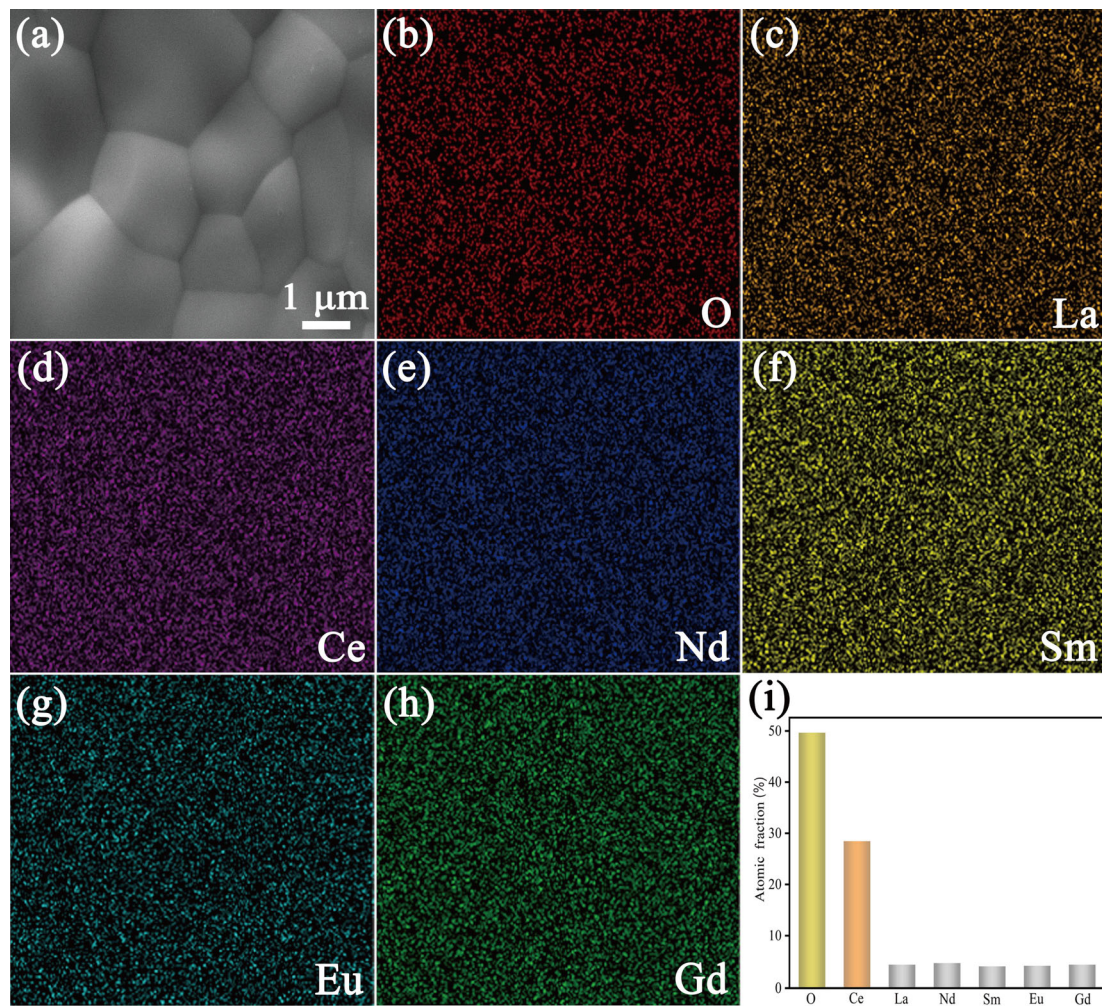
Fig. 5 (a) SEM image of bulk $(La_{0.2}Nd_{0.2}Sm_{0.2}Eu_{0.2}Gd_{0.2})_2Ce_2O_7$; (b–h) corresponding EDS mappings of O, La, Ce, Nd, Sm, Eu, and Gd elements, respectively; (i) atomic fraction of as-prepared bulk specimen.
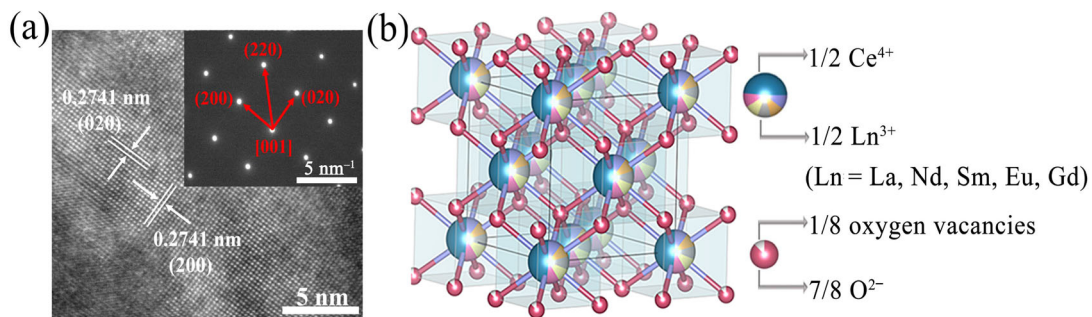
Fig. 6 Microstructure characterizations of bulk $(La_{0.2}Nd_{0.2}Sm_{0.2}Eu_{0.2}Gd_{0.2})_2Ce_2O_7$: (a) HRTEM and SAED patterns; (b) schematic of three-dimensional structure.

crystal. The existence of a large amount of oxygen vacancies greatly influences the phonon scattering, which will directly affect the thermal conductivity. Besides, the randomly distributed multiple rare earth ions may further affect the thermal properties of high-entropy $(La_{0.2}Nd_{0.2}Sm_{0.2}Eu_{0.2}Gd_{0.2})_2Ce_2O_7$, which will be discussed in the following.

3. 3 Thermo-physical properties of high-entropy $(La_{0.2}Nd_{0.2}Sm_{0.2}Eu_{0.2}Gd_{0.2})_2Ce_2O_7$

Thermal conductivity and TEC are critical parameters to evaluate the performance of TBCs. Currently, the thermal conductive properties of a number of high-entropy ceramics have been reported for TBCs. However,

the relatively high thermal conductivity and low TECs are urgently needed to be improved. Moreover, the research on thermal contraction behavior of cerium oxide-based high-entropy oxides is still a lack of deep study. In this work, we carried out a series of measurements to estimate these thermo-physical properties of $(La_{0.2}Nd_{0.2}Sm_{0.2}Eu_{0.2}Gd_{0.2})_2Ce_2O_7$. All the testing results indicate that the as-synthesized material can be regarded as a potential thermal barrier material.

Through the characterizations of thermal properties, the specific heat capacity, thermal diffusivity, and thermal conductivity of $(La_{0.2}Nd_{0.2}Sm_{0.2}Eu_{0.2}Gd_{0.2})_2Ce_2O_7$ are summarized in Fig. 7(a). According to Neumann–Kopp rule, the heat capacity (C_p) can be obtained by summation of the heat capacity of constituent rare earth oxides. The calculated heat capacity is plotted in black line. It can be seen that C_p (0.34–0.47 $J \cdot g^{-1} \cdot K^{-1}$) increases with the temperature rising from 25 to 1400 ℃, which is lower than that of YSZ (0.45–0.65 $J \cdot g^{-1} \cdot K^{-1}$ from room temperature to 1200 ℃) [45]. The increase of specific heat capacity with the rise of temperature mainly attributes to the fact of large volume expansion and enhanced phonon scattering [32]. The heat capacity at constant pressure (C_p) and the Debye model are

applied to evaluate the heat capacity at constant volume (C_V). The relation between the two heat capacities (C_V and C_p) can be expressed through $C_p = C_V + \alpha^2 V(T)TB_0$, where α is the volumetric TEC, $V(T)$ is the equilibrium cell volume at temperature T, and B_0 is the isothermal bulk modulus. According to the Debye model, C_V will reach a constant beyond Debye temperature. Thus, C_p increases linearly with the increase of temperature [46].

The green curve describes the thermal diffusivity of $(La_{0.2}Nd_{0.2}Sm_{0.2}Eu_{0.2}Gd_{0.2})_2Ce_2O_7$ varying from 25 to 1400 ℃. Contrary to the heat capacity, the thermal diffusivity obeys the T^{-1} law at low temperature, where the thermal diffusivity descends with the increase of temperature. The high-disordered high-entropy configuration of $(La_{0.2}Nd_{0.2}Sm_{0.2}Eu_{0.2}Gd_{0.2})_2Ce_2O_7$ can significantly strengthen inharmonic lattice vibration, enhance phonon scattering, and lead to a great reduction in thermal diffusivity. With the temperature rising up, it is worth noting that the thermal diffusivity is observed to show a slight ascension from 1200 ℃. Such slightly growing of diffusivity results from high-temperature heat radiation. Accordingly, in addition to low thermal diffusivity, $(La_{0.2}Nd_{0.2}Sm_{0.2}Eu_{0.2}Gd_{0.2})_2Ce_2O_7$ is verified to have an excellent heat radiation resistance at high
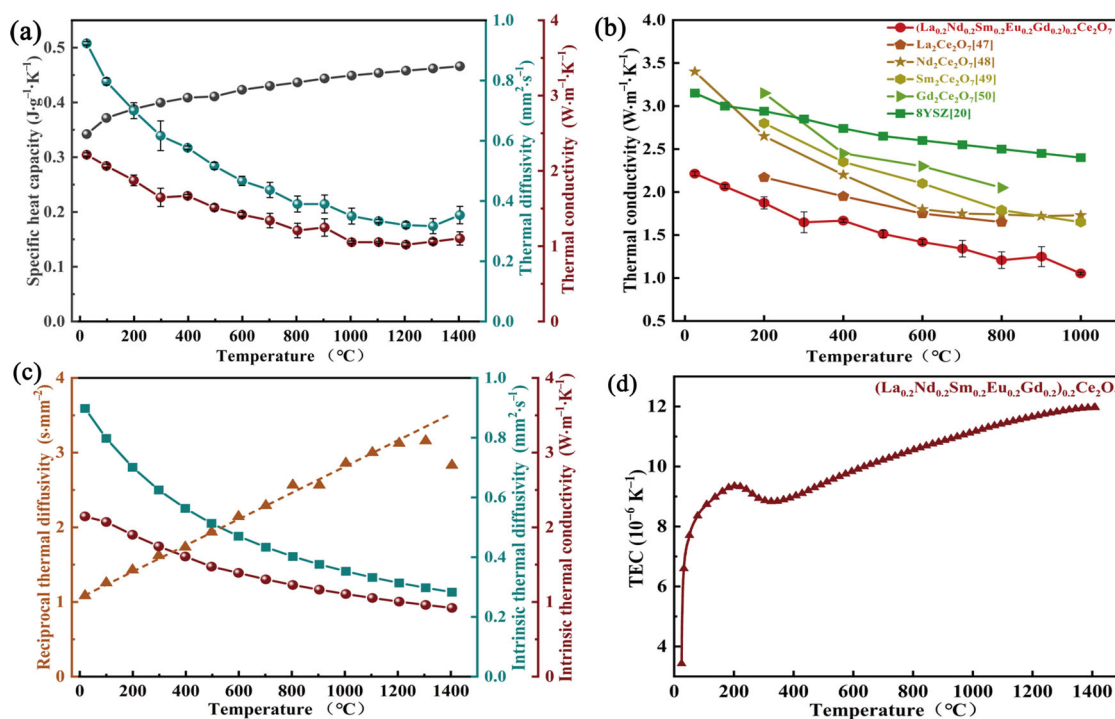
Fig. 7 Temperature dependent thermal properties of bulk $(La_{0.2}Nd_{0.2}Sm_{0.2}Eu_{0.2}Gd_{0.2})_2Ce_2O_7$. (a) Specific heat capacity (dark grey curve), thermal diffusivity (green curve), and thermal conductivity (red curve). (b) Thermal conductivities of as-prepared material, $Ln_2Ce_2O_7$, and 8YSZ. (c) Calculated reciprocal intrinsic thermal diffusivity (brown curve), fitted reciprocal intrinsic thermal diffusivity (brown dotted line), calculated intrinsic thermal diffusivity (green curve), and intrinsic thermal conductivity (red curve). (d) TEC.

temperature. The demonstration of T^{-1} law is presented in the discussion part of thermal conductivity below.

The red curve in Fig. 7(a) depicts the thermal conductivity of $(La_{0.2}Nd_{0.2}Sm_{0.2}Eu_{0.2}Gd_{0.2})_2Ce_2O_7$. When the temperature rises from 25 to 1200 ℃, the thermal conductivity drops down from 2.21 to 1.02 W·m⁻¹·K⁻¹, and then increases gradually to 1.10 W·m⁻¹·K⁻¹ at 1400 ℃. Similar to thermal diffusivity, the thermal conductivity of $(La_{0.2}Nd_{0.2}Sm_{0.2}Eu_{0.2}Gd_{0.2})_2Ce_2O_7$ decreases with the increase of temperature. Likewise, it can be clearly observed that the thermal conductivity slightly rises up from 1200 ℃, which attributes to the thermal radiation effect. For comparison, the thermal conductivities of constituent $Ln_2Ce_2O_7$ and 8YSZ are illustrated in Fig. 7(b). Evidently, the thermal conductivity of the as-synthesized material at 800 ℃ (1.21 W·m⁻¹·K⁻¹) is much lower than those of simple constituent cerates (1.65–2.05 W·m⁻¹·K⁻¹ at 800 ℃) [47–50] and conventional 8YSZ (2.50 W·m⁻¹·K⁻¹ at 800 ℃) [20]. Such outstanding thermal insulation performance of the material synthesized in this work can be explained by Debye's phonon theory, where the thermal conductivity can be reduced by phonon scattering for insulating materials. Here, the thermal conductivity is expressed by Eq. (3) [51]:

$$\kappa = \frac{C_V \times l \times V_M}{3} \qquad (3)$$

where C_V is the specific heat capacity, l represents the phonon mean free path, and V_M is related to the mean acoustic velocity. According to Dulong–Petit rule, C_V will rise up to its upper limit $3k_B$ beyond Debye's temperature. Besides, V_M is determined by the intrinsic inter-atomic reaction of the materials. Therefore, due to the limited impact of C_V on thermal conductivity, κ is dominated by the phonon mean free path l. Based on the explanations above, low thermal conductivity mainly depends on short mean free path, which largely relies on strong phonon scattering. The phonon mean free path under certain frequency (ω) and temperature (T) can be defined by Eq. (4) [52,53]:

$$1/l(\omega,T) = 1/l_i + 1/l_b + 1/l_d \qquad (4)$$

where l_i, l_b, and l_d represent the phonon mean free path of intrinsic scattering from lattice structure, grain boundary scattering, and point defect scattering (such as oxygen vacancy and cation vacancy), respectively. The phonon scattering for insulating substances is mainly determined by their intrinsic crystal structure. In this work, the average grain size of $(La_{0.2}Nd_{0.2}Sm_{0.2}Eu_{0.2}Gd_{0.2})_2Ce_2O_7$

(measured to be around 3.1 μm from SEM images) is dramatically larger than that of phonon mean free path (in nano scale), and thus the grain boundary scattering can be neglected. It is claimed that the phonon mean free path of point defect scattering and grain boundary scattering is a temperature-independent constant. Thus, the phonon mean free path is dominated by the phonon–phonon scattering process from intrinsic scattering. The relation between l and T can be expressed as below [54,55]:

$$\frac{1}{l(\omega,T)} \sim \left(\frac{bCn^{1/3}}{T_D}\right)T + \left(D - \frac{1}{2}C\right) \qquad (5)$$

where b, C, and D are constants, n is the atom number per primitive cell, and T_D is the Debye temperature. According to the Debye model, thermal diffusivity (λ) can be calculated by Eq. (6):

$$\lambda = \frac{1}{3}V_M l \qquad (6)$$

Since V_M is temperature independent, thermal diffusivity can be approximated as

$$\frac{1}{\lambda} \sim \frac{1}{l(\omega,T)} \sim \left(\frac{bCn^{1/3}}{T_D}\right)T + \left(D - \frac{1}{2}C\right) \qquad (7)$$

Obviously, the reciprocal thermal diffusivity (λ^{-1}) is proportional to temperature (T).

According to the discussions above, the calculated λ^{-1} is plotted with brown triangles in Fig. 7(c). It can be seen that λ^{-1} increases linearly with the increase of temperatures (T^{-1} law) with a fitted relation of $\lambda^{-1} = 0.00175T + 0.60084$ in dotted brown line. Notably, λ^{-1} deviates from the linear line beyond 1200 ℃ and decreases gradually, which suggests a prominent thermal radiation resistance of $(La_{0.2}Nd_{0.2}Sm_{0.2}Eu_{0.2}Gd_{0.2})_2Ce_2O_7$. Intrinsic thermal diffusivity recalculated by substituting fitted λ^{-1} into Eq. (2) is illustrated with the green curve in Fig. 7(c). It decreases smoothly from 0.90 to 0.28 mm²·s⁻¹ in the range of room temperature to 1400 ℃. Based on these results, the minimum intrinsic thermal conductivity is calculated to be 0.92 W·m⁻¹·K⁻¹ at 1400 ℃ after removing the thermal radiation effect, which is displayed with the red line in Fig. 7(c). In conclusion, the low conductivity of the as-prepared material can be concluded by three reasons as follows. First, the impact of point defect scattering (oxygen vacancy) on the thermal conductivity of $(La_{0.2}Nd_{0.2}Sm_{0.2}Eu_{0.2}Gd_{0.2})_2Ce_2O_7$ is vitally essential, especially oxygen vacancies. It can be theoretically deduced that the concentration of

oxygen vacancy in our material reaches a high proportion of around 12.5%, which is demonstrated to be the strongest scattering center among point defect scattering. As a result, the thermal conductivity is greatly decreased. Another reason is the strengthened phonon scattering from the cocktail effect of HECs. The disordered elemental distribution contributes to enhancing the synergistic effect of multicomponent elements and increasing the number of scattering centers. Finally, acknowledged by Clarke's principle for the selection of TBCs, materials with expected low thermal conductivity commonly exhibit four principal characteristics, including high atomic mass, complex structure, a collection of diverse atoms per molecule, and non-directional bonding [51]. The fabricated high-entropy ceramic in this work just satisfies well with the descriptions above with multicomponent elements randomly distributed in unit cell.

TEC is regarded as another significant property for the assessment of thermal barrier materials. In practical application, serious TEC mismatch between ceramic top coat and bond coat (MCrAlY, $(13.0\text{–}16.0) \times 10^{-6}$ K^{-1}, M = γNi or Co matrix) leads to overlarge thermal stress, resulting crack and failure of TBCs [56]. Figure 7(d) presents the TEC of $(La_{0.2}Nd_{0.2}Sm_{0.2}Eu_{0.2}Gd_{0.2})_2Ce_2O_7$ as a function of temperature. With temperature rising to 1400 ℃, TEC reaches a value of approximately 12.0 $\times 10^{-6}$ K^{-1}.

The extensive application of commercial 8YSZ is terribly impeded by the disruptive t–m phase transformation beyond 1200 ℃. Therefore, in addition to high TEC, a stable crystal structure of thermal insulation material also plays a crucial role in TBCs. In this work, the phase transition of $(La_{0.2}Nd_{0.2}Sm_{0.2}Eu_{0.2}Gd_{0.2})_2Ce_2O_7$ is investigated in the process of temperature rising through high-temperature *in-situ* XRD equipment. As can be seen from Fig. 8(a), there are no impurity peaks

observed from the XRD patterns at all temperatures. Furthermore, with temperature rising from 27 to 1400 ℃, no phase transformation can be observed, which indicates an outstanding high-temperature phase stability of the prepared material. The peak at around 40° is the characteristic peak of Pt which origins from the test holder. The crystal plane of (200) locating at around 32.26° is enlarged in Fig. 8(b). It is clear that the peak position shifts gradually to lower 2θ degree without obvious intensity change. According to Bragg's diffraction equation:

$$2d\sin\theta = n\lambda \qquad (8)$$

where λ is the wavelength of the Cu Kα in this work, *d* is the spacing of the crystal planes, and *n* is an integer. When θ decreases with the peak shifting to lower diffraction degree direction, the interplanar spacing of (200) plane becomes larger subsequently. The gradual increasing distance of crystal plane suggests a stable expansion in lattice volume, thus leading to steady thermal expansion behaviour in $(La_{0.2}Nd_{0.2}Sm_{0.2}Eu_{0.2}Gd_{0.2})_2Ce_2O_7$.

In-situ XRD is performed from 27 to 390 ℃ to study the thermal contraction of the as-prepared material. As displayed in Fig. 9(a), there is no impurity peak detected in the testing temperature range. Furthermore, no phase transition occurs in the thermal contraction process. In order to get a deep insight into this issue, the cell parameters are calculated from the data of *in-situ* XRD, and the results are displayed in Fig. 9(b). It can be seen that the cell parameter increases gradually from 27 to 240 ℃. However, when the temperature exceeds 240 ℃, the cell parameter sharply drops down and rises again after 250 ℃, and increases stably with the temperature rising, which possibly originates from the valence state transition of cerium ions. The results above further prove the stable phase stability of our prepared material.

TEC vs. thermal conductivity of the reported TBCs is summarized in Fig. 10. Compared with TEC reported in the literature for other TBCs like 8YSZ (10.9×10^{-6} K^{-1}) [20], $La_2Zr_2O_7$ ($\sim 9 \times 10^{-6}$ K^{-1}) [33], $SmNbO_4$ ($\sim 11.1 \times 10^{-6}$ K^{-1}) [57], etc. [46,55,57–62], our prepared material shows a much higher TEC, which greatly contributes to reducing thermal stress and prolonging service life of TBC. Interestingly, $(La_{0.2}Nd_{0.2}Sm_{0.2}Eu_{0.2}Gd_{0.2})_2Ce_2O_7$ presents a slight thermal contraction in the range of 200–300 ℃. In comparison with other materials, the TEC only drops down from 9.2×10^{-6} to 8.7×10^{-6} K^{-1}, while the
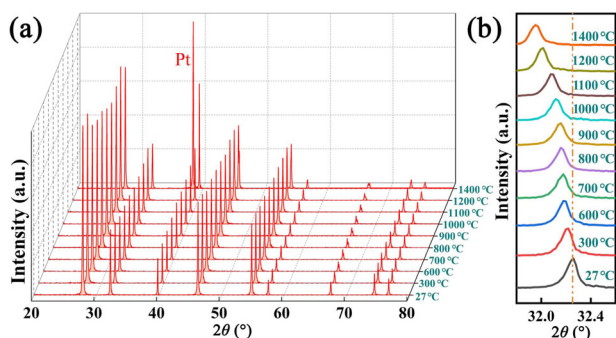
Fig. 8 (a) High-temperature *in-situ* XRD patterns; (b) corresponding XRD patterns of enlarged (200) peak.
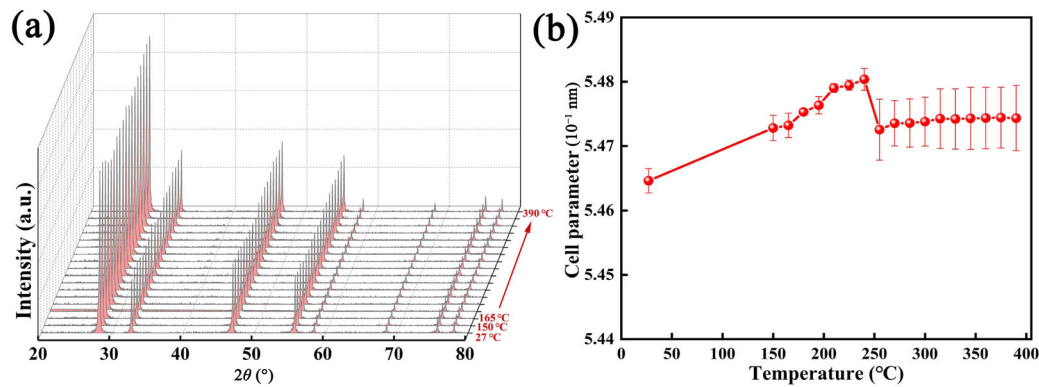
Fig. 9 (a) High-temperature *in-situ* XRD patterns from room temperature to 390 ℃ and (b) corresponding calculated cell parameters.
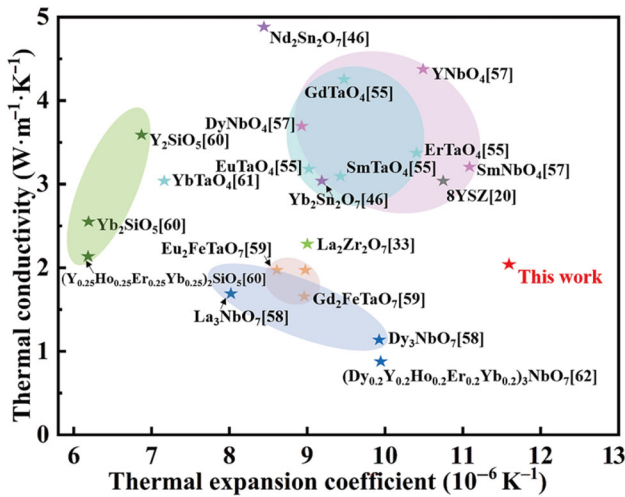
Fig. 10 Thermal conductivity vs. TEC of typical TBC materials. The thermal conductivities are measured at room temperature, except $EuTaO_4$, $ErTaO_4$, $SmTaO_4$, $GdTaO_4$ (100 ℃) and Eu_2FeTaO_7, Gd_2FeTaO_7 (50 ℃). The value of TEC is collected at 1200 ℃, except 8YSZ (1000 ℃), $Yb_2Sn_2O_7$ (1300 ℃), and $Nd_2Sn_2O_7$ (1300 ℃).

$La_2Ce_2O_7$ [30] has an extremely large change of TEC from 9×10^{-6} to -5×10^{-6} K^{-1}. Likewise, the TEC of $EuTa_3O_9$ sharply falls down from 10×10^{-6} to 2.5×10^{-6} K^{-1} [56], and $NdTa_3O_9$ also shows a heavy negative thermal expansion [56]. The mechanisms for thermal contraction have not been cleared currently, but the most possible explanation is the thermal rotation of coordination polyhedrons and shearing motion of M–O–M' (M, M' = metal atom) [30]. Above all, the high TEC and marginal thermal contraction of $(La_{0.2}Nd_{0.2}Sm_{0.2}Eu_{0.2}Gd_{0.2})_2Ce_2O_7$ will provide a perfect TEC match with bond coat, and avoid failure of TBC system dramatically.

In addition, the hardness of $(La_{0.2}Nd_{0.2}Sm_{0.2}Eu_{0.2}Gd_{0.2})_2Ce_2O_7$ was measured to be 8.72 GPa, which is lower than that of YSZ (10.75 GPa) but higher than that of $La_2Ce_2O_7$ (5.57 GPa) [63]. A suitable hardness of TBCs contributes to extending the working life of TBCs. Compared with single component $La_2Ce_2O_7$, such relatively high hardness for high-entropy $(La_{0.2}Nd_{0.2}Sm_{0.2}Eu_{0.2}Gd_{0.2})_2Ce_2O_7$ mainly attributes to solid solution strengthening of multicomponent configuration. In practical application, high hardness of TBCs can protect the hot-end component from direct friction and strike from foreign substances. Meanwhile, on the other hand, a relatively low hardness can contribute to enhancing the thermal tolerance from residual stress and restricting the propagation of cracks.

4   Conclusions

High-entropy $(La_{0.2}Nd_{0.2}Sm_{0.2}Eu_{0.2}Gd_{0.2})_2Ce_2O_7$ is successfully synthesized by a two-step solid-state reaction method. The thermo-physical property of $(La_{0.2}Nd_{0.2}Sm_{0.2}Eu_{0.2}Gd_{0.2})_2Ce_2O_7$ applied as TBC is studied in this work. According to the results of characterizations, the prepared material presents prominent thermal insulation behavior as the intrinsic thermal conductivity reaches a low value of 0.92 $W·m^{-1}·K^{-1}$ at 1400 ℃. The cocktail effect of high-entropy oxides plays a vitally critical role in the reduction of thermal conductivity. The high content oxygen vacancies and randomly distributed multicomponent rare earth ions greatly increase the number of phonon scattering centers, and thus strengthen phonon scattering. As a result, the thermal conductivity is weakened to a great extent. In addition, $(La_{0.2}Nd_{0.2}Sm_{0.2}Eu_{0.2}Gd_{0.2})_2Ce_2O_7$ possesses a high TEC of 12.0×10^{-6} K^{-1} up to 1400 ℃. All the prominent properties above render high-entropy $(La_{0.2}Nd_{0.2}Sm_{0.2}Eu_{0.2}Gd_{0.2})_2Ce_2O_7$ a potential candidate for thermal barrier material.

Acknowledgements

References

[1] Rost CM, Sachet E, Borman T, *et al*. Entropy-stabilized oxides. *Nat Commun* 2015, **6**: 8485.

[2] Sarker P, Harrington T, Toher C, *et al*. High-entropy high-hardness metal carbides discovered by entropy descriptors. *Nat Commun* 2018, **9**: 4980.

[3] Harrington TJ, Gild J, Sarker P, *et al*. Phase stability and mechanical properties of novel high entropy transition metal carbides. *Acta Mater* 2019, **166**: 271–280.

[4] Rost CM, Borman T, Hossain MD, *et al*. Electron and phonon thermal conductivity in high entropy carbides with variable carbon content. *Acta Mater* 2020, **196**: 231–239.

[5] Jin T, Sang XH, Unocic RR, *et al*. Mechanochemical-assisted synthesis of high-entropy metal nitride via a soft urea strategy. *Adv Mater* 2018, **30**: 1707512.

[6] Gild J, Zhang YY, Harrington T, *et al*. High-entropy metal diborides: A new class of high-entropy materials and a new type of ultrahigh temperature ceramics. *Sci Rep* 2016, **6**: 37946.

[7] Feng L, Fahrenholtz WG, Hilmas GE. Processing of dense high-entropy boride ceramics. *J Eur Ceram Soc* 2020, **40**: 3815–3823.

[8] Zhang RZ, Gucci F, Zhu H, *et al*. Data-driven design of ecofriendly thermoelectric high-entropy sulfides. *Inorg Chem* 2018, **57**: 13027–13033.

[9] Qin Y, Liu JX, Li F, *et al*. A high entropy silicide by reactive spark plasma sintering. *J Adv Ceram* 2019, **8**: 148–152.

[10] Qin Y, Wang JC, Liu JX, *et al*. High-entropy silicide ceramics developed from (TiZrNbMoW)Si$_2$ formulation doped with aluminum. *J Eur Ceram Soc* 2020, **40**: 2752–2759.

[11] Xiang HM, Xing Y, Dai FZ, *et al*. High-entropy ceramics: Present status, challenges, and a look forward. *J Adv Ceram* 2021, **10**: 385–441.

[12] Wang QS, Sarkar A, Wang D, *et al*. Multi-anionic and -cationic compounds: New high entropy materials for advanced Li-ion batteries. *Energy Environ Sci* 2019, **12**: 2433–2442.

[13] Ghigna P, Airoldi L, Fracchia M, *et al*. Lithiation mechanism in high-entropy oxides as anode materials for Li-ion batteries: An operando XAS study. *ACS Appl Mater Interfaces* 2020, **12**: 50344–50354.

[14] Lun ZY, Ouyang B, Kwon DH, *et al*. Cation-disordered rocksalt-type high-entropy cathodes for Li-ion batteries. *Nat Mater* 2021, **20**: 214–221.

[15] Jiang B, Yu Y, Cui J, *et al*. High-entropy-stabilized chalcogenides with high thermoelectric performance. *Science* 2021, **371**: 830–834.

[16] Chen H, Xiang HM, Dai FZ, *et al*. High entropy (Yb$_{0.25}$Y$_{0.25}$Lu$_{0.25}$Er$_{0.25}$)$_2$SiO$_5$ with strong anisotropy in thermal expansion. *J Mater Sci Technol* 2020, **36**: 134–139.

[17] Zhao ZF, Chen H, Xiang HM, *et al*. High entropy defective fluorite structured rare-earth niobates and tantalates for thermal barrier applications. *J Adv Ceram* 2020, **9**: 303–311.

[18] Ren K, Wang QK, Shao G, *et al*. Multicomponent high-entropy zirconates with comprehensive properties for advanced thermal barrier coating. *Scripta Mater* 2020, **178**: 382–386.

[19] Lashmi PG, Ananthapadmanabhan PV, Unnikrishnan G, *et al*. Present status and future prospects of plasma sprayed multilayered thermal barrier coating systems. *J Eur Ceram Soc* 2020, **40**: 2731–2745.

[20] Zhao M, Ren XR, Yang J, *et al*. Thermo-mechanical properties of ThO$_2$-doped Y$_2$O$_3$ stabilized ZrO$_2$ for thermal barrier coatings. *Ceram Int* 2016, **42**: 501–508.

[21] Cao XQ, Vassen R, Tietz F, *et al*. New double-ceramic-layer thermal barrier coatings based on zirconia–rare earth composite oxides. *J Eur Ceram Soc* 2006, **26**: 247–251.

[22] Dwivedi G, Viswanathan V, Sampath S, *et al*. Fracture toughness of plasma-sprayed thermal barrier ceramics: Influence of processing, microstructure, and thermal aging. *J Am Ceram Soc* 2014, **97**: 2736–2744.

[23] Ren XR, Pan W. Mechanical properties of high-temperature-degraded yttria-stabilized zirconia. *Acta Mater* 2014, **69**: 397–406.

[24] Xing C, Yi MY, Shan X, *et al*. Sintering behavior of a nanostructured thermal barrier coating deposited using electro-sprayed particles. *J Am Ceram Soc* 2020, **103**: 7267–7282.

[25] Limarga AM, Shian S, Baram M, *et al*. Effect of high-temperature aging on the thermal conductivity of nanocrystalline tetragonal yttria-stabilized zirconia. *Acta Mater* 2012, **60**: 5417–5424.

[26] Tan Y, Longtin JP, Sampath S, *et al*. Effect of the starting microstructure on the thermal properties of as-sprayed and thermally exposed plasma-sprayed YSZ coatings. *J Am Ceram Soc* 2009, **92**: 710–716.

[27] Wang YX, Zhou CG. Hot corrosion behavior of nanostructured Gd$_2$O$_3$ doped YSZ thermal barrier coating in presence of Na$_2$SO$_4$ + V$_2$O$_5$ molten salts. *Prog Nat Sci Mater Int* 2017, **27**: 507–513.

[28] Wei QL, Guo HB, Gong SK. Microstructure evolution of Nd$_2$O$_3$ and Yb$_2$O$_3$ co-doped YSZ thermal barrier coatings during high temperature exposure. *Mater Sci Forum* 2007, **546–549**: 1735–1738.

[29] Wang Q, Guo L, Yan Z, *et al*. Phase composition, thermal conductivity, and toughness of TiO$_2$-doped, Er$_2$O$_3$-stabilized ZrO$_2$ for thermal barrier coating applications. *Coatings* 2018, **8**: 253.

[30] Cao XQ, Vassen R, Fischer W, *et al*. Lanthanum–cerium oxide as a thermal barrier-coating material for high-temperature applications. *Adv Mater* 2003, **15**: 1438–1442.

[31] Shen ZY, Liu GX, Mu RD, *et al*. Effects of Er stabilization on thermal property and failure behavior of $Gd_2Zr_2O_7$ thermal barrier coatings. *Corros Sci* 2021, **185**: 109418.

[32] Wang J, Chong XY, Zhou R, *et al*. Microstructure and thermal properties of $RETaO_4$ (RE = Nd, Eu, Gd, Dy, Er, Yb, Lu) as promising thermal barrier coating materials. *Scripta Mater* 2017, **126**: 24–28.

[33] Wang CJ, Wang Y. Thermophysical properties of $La_2(Zr_{0.7}Ce_{0.3})_2O_7$ prepared by hydrothermal synthesis for nano-sized thermal barrier coatings. *Ceram Int* 2015, **41:** 4601–4607.

[34] Zhang RZ, Reece MJ. Review of high entropy ceramics: Design, synthesis, structure and properties. *J Mater Chem A* 2019, **7**: 22148–22162.

[35] Braun JL, Rost CM, Lim M, *et al*. Charge-induced disorder controls the thermal conductivity of entropy-stabilized oxides. *Adv Mater* 2018, **30**: 1805004.

[36] Wright AJ, Wang QY, Ko ST, *et al*. Size disorder as a descriptor for predicting reduced thermal conductivity in medium-and high-entropy pyrochlore oxides. *Scripta Mater* 2020, **181**: 76–81.

[37] Zhao ZF, Xiang HM, Dai FZ, *et al*. $(La_{0.2}Ce_{0.2}Nd_{0.2}Sm_{0.2}Eu_{0.2})_2Zr_2O_7$: A novel high-entropy ceramic with low thermal conductivity and sluggish grain growth rate. *J Mater Sci Technol* 2019, **35**: 2647–2651.

[38] Chen H, Zhao ZF, Xiang HM, *et al*. High entropy $(Y_{0.2}Yb_{0.2}Lu_{0.2}Eu_{0.2}Er_{0.2})_3Al_5O_{12}$: A novel high temperature stable thermal barrier material. *J Mater Sci Technol* 2020, **48**: 57–62.

[39] Ren K, Wang QK, Cao YJ, *et al*. Multicomponent rare-earth cerate and zirconocerate ceramics for thermal barrier coating materials. *J Eur Ceram Soc* 2021, **41**: 1720–1725.

[40] Schlichting KW, Padture NP, Klemens PG. Thermal conductivity of dense and porous yttria-stabilized zirconia. *J Mater Sci* 2001, **36**: 3003–3010.

[41] Che JW, Wang XZ, Liu XY, *et al*. Thermal transport property in pyrochlore-type and fluorite-type $A_2B_2O_7$ oxides by molecular dynamics simulation. *Int J Heat Mass Transf* 2022, **182:** 122038.

[42] Yamamura H, Nishino H, Kakinuma K, *et al*. Crystal phase and electrical conductivity in the pyrochlore-type composition systems, $Ln_2Ce_2O_7$ (Ln = La, Nd, Sm, Eu, Gd, Y and Yb). *J Ceram Soc Jpn* 2003, **111**: 902–906.

[43] Shannon RD. Revised effective ionic radii and systematic studies of interatomic distances in halides and chalcogenides. *Acta Crystallogr Sect A* 1976, **32**: 751–767.

[44] Teng Z, Tan YQ, Zeng SF, *et al*. Preparation and phase evolution of high-entropy oxides $A_2B_2O_7$ with multiple elements at A and B sites. *J Eur Ceram Soc* 2021, **41**: 3614–3620.

[45] Zhang YL, Guo L, Yang YP, *et al*. Influence of Gd_2O_3 and Yb_2O_3 co-doping on phase stability, thermo-physical properties and sintering of 8YSZ. *Chin J Aeronaut* 2012, **25**: 948–953.

[46] Feng J, Xiao B, Zhou R, *et al*. Thermal expansion and conductivity of $RE_2Sn_2O_7$ (RE = La, Nd, Sm, Gd, Er and Yb) pyrochlores. *Scripta Mater* 2013, **69**: 401–404.

[47] Zhang HS, Wei Y, Li G, *et al*. Investigation about thermal conductivities of $La_2Ce_2O_7$ doped with calcium or magnesium for thermal barrier coatings. *J Alloys Compd* 2012, **537**: 141–146.

[48] Zhong XH, Xu ZH, Zhang YF, *et al*. Phase stability and thermophysical properties of neodymium cerium composite oxide. *J Alloys Compd* 2009, **469**: 82–88.

[49] Zhang HS, Zhao LM, Sang WW, *et al*. Thermophysical performances of $(La_{1/6}Nd_{1/6}Yb_{1/6}Y_{1/6}Sm_{1/6}Lu_{1/6})_2Ce_2O_7$ high-entropy ceramics for thermal barrier coating applications. *Ceram Int* 2022, **48**: 1512–1521.

[50] Zhang HS, Liao SR, Dang XD, *et al*. Preparation and thermal conductivities of $Gd_2Ce_2O_7$ and $(Gd_{0.9}Ca_{0.1})_2Ce_2O_{6.9}$ ceramics for thermal barrier coatings. *J Alloys Compd* 2011, **509**: 1226–1230.

[51] Clarke DR. Materials selection guidelines for low thermal conductivity thermal barrier coatings. *Surf Coat Technol* 2003, **163–164**: 67–74.

[52] Klemens PG. The scattering of low-frequency lattice waves by static imperfections. *Proc Phys Soc A* 1955, **68**: 1113–1128.

[53] Callaway J, von Baeyer HC. Effect of point imperfections on lattice thermal conductivity. *Phys Rev* 1960, **120**: 1149–1154.

[54] Tian ZL, Lin CF, Zheng LY, *et al*. Defect-mediated multiple-enhancement of phonon scattering and decrement of thermal conductivity in $(Y_xYb_{1-x})_2SiO_5$ solid solution. *Acta Mater* 2018, **144**: 292–304.

[55] Chen L, Hu MY, Wu P, *et al*. Thermal expansion performance and intrinsic lattice thermal conductivity of ferroelastic $RETaO_4$ ceramics. *J Am Ceram Soc* 2019, **102**: 4809–4821.

[56] Chen L, Jiang YH, Chong XY, *et al*. Synthesis and thermophysical properties of $RETa_3O_9$ (RE = Ce, Nd, Sm, Eu, Gd, Dy, Er) as promising thermal barrier coatings. *J Am Ceram Soc* 2018, **101**: 1266–1278.

[57] Wu FS, Wu P, Zhou YX, *et al*. The thermo-mechanical properties and ferroelastic phase transition of $RENbO_4$ (RE = Y, La, Nd, Sm, Gd, Dy, Yb) ceramics. *J Am Ceram Soc* 2020, **103**: 2727–2740.

[58] Chen L, Wu P, Song P, *et al*. Potential thermal barrier coating materials: RE_3NbO_7 (RE = La, Nd, Sm, Eu, Gd, Dy) ceramics. *J Am Ceram Soc* 2018, **101**: 4503–4508.

[59] Zheng Q, Chen L, Song P, *et al*. Potential thermal barrier coating materials: RE_2FeTaO_7 (RE = Y, Eu, Gd, Dy) compounds. *J Alloys Compd* 2021, **855**: 157408.

[60] Ren XM, Tian ZL, Zhang J, *et al*. Equiatomic quaternary $(Y_{1/4}Ho_{1/4}Er_{1/4}Yb_{1/4})_2SiO_5$ silicate: A perspective multifunctional thermal and environmental barrier coating material. *Scripta Mater* 2019, **168**: 47–50.

[61] Chen L, Hu MY, Guo J, *et al*. Mechanical and thermal properties of $RETaO_4$ (RE = Yb, Lu, Sc) ceramics with monoclinic-prime phase. *J Mater Sci Technol* 2020, **52**: 20–28.

[62] Zhu JT, Meng XY, Xu J, *et al*. Ultra-low thermal

conductivity and enhanced mechanical properties of high-entropy rare earth niobates (RE_3NbO_7, RE = Dy, Y, Ho, Er, Yb). *J Eur Ceram Soc* 2021, **41**: 1052–1057.

[63] Dehkharghani AMF, Rahimipour MR, Zakeri M. Improving the thermal shock resistance and fracture toughness of synthesized $La_2Ce_2O_7$ thermal barrier coatings through formation of $La_2Ce_2O_7$/YSZ composite coating via air plasma spraying. *Surf Coat Technol* 2020, **399**: 126174.